

Localized overheating on aluminum metafilms mediated by surface plasmons

D. E. Martínez-Lara^{a,*}, R. González-Campuzano^{a,c}, J. L. Benítez^b and D. Mendoza^{a,**}

^a*Instituto de Investigaciones en Materiales, Universidad Nacional Autónoma de México, Apartado Postal 70-360, Ciudad de México 04510, México.*

*e-mail: *davideduardo@ciencias.unam.mx; **doroteo@unam.mx*

^b*Instituto de Ciencias Aplicadas y Tecnología, Universidad Nacional Autónoma de México, Apartado Postal 70-186, Ciudad de México 04510, México.*

^c*Current affiliation is b*

Received 18 February 2021; accepted 10 April 2021

We studied the increase in temperature of systems formed by thin aluminum films deposited on texturized substrates which we denominated aluminum metafilms. By varying the geometric parameters of the metafilms, surface plasmons in the wavelength range of ~ 420 -770 nm were excited. Temperature measurements as a function of the intensity of incident radiation in the interval from 0 to 4×10^{18} photons/(s)cm² using wavelengths of 445, 532 and 650 nm, showed temperature increases up to ~ 200 K, these attributed to metafilm morphology and hot electrons result of the non-radiative decay of the surface plasmons. Also, increases from $\sim 1.3 \times 10^{-6}$ Ω cm to 2.3×10^{-2} Ω cm in the electrical resistivity were recorded, when the metafilms were irradiated for times of 1 s; when the exposure times were greater than 4 s, irreversibly changes in the morphology of the samples were observed.

Keywords: Surface Plasmons; Metamaterials; Aluminum; nanostructures.

PACS: 73.20.Mf; 81.05.Xj; 78.67.Pt; 73.50.-h; 68.60.Dv

DOI: <https://doi.org/10.31349/RevMexFis.67.051001>

1. Introduction

Surface plasmons (SP) are collective oscillations of charge located between the surface of a dielectric and a metal [1], which have made it possible to improve and reduce the dimensions of electronic devices [2-4]. In biomedicine, they are being used in photothermal therapies and cancer treatments [5,6], as well as their use to convert solar energy into chemical energy [7]. Recent studies have shown that systems formed by plasmonic nanostructures can be used as nano heat sources [8,9].

Among the traditionally used metals in plasmonics, silver (Ag) and gold (Au) stand out, because they have a wide range of the electromagnetic spectrum in which SP can be excited, ranging from infrared (IR) to visible (Vis) with energy losses at ~ 318 nm and ~ 517 nm as a result of their interband transitions (IT) [10,11] respectively.

On the other hand, aluminum (Al) is a metal that has begun to be explored for plasmonic applications [12,13], which in comparison with Ag and Au, has some advantages, such as a broader SP excitation range that goes from ultraviolet (UV) to IR; it has a layer of native self-limited oxide $\sim 3 - 4$ nm [14] that protects it from corrosive environments, as well as being cheaper. Due to its high density energy, it can release large amounts of energy through the SP-assisted combustion process (a phenomenon known as photo-ignition), which can be applied for the development of nanosolders, nano propulsors or nanoexplosives [15].

Zheng *et al.* [16] have shown that hot carriers (hot electrons) induced by plasmons, can be used in two-dimensional structures to generate photocurrents [17], with the capacity to

transfer their energy to phonons [5], producing temperature increases in nanometric areas in a matter of femtoseconds [18].

It has recently been shown that it is possible to excite SP at certain wavelengths by varying the metal nanostructures dimensions of Al, Pb, and Ag [19-21]. In this work, Al thin films have been deposited on nanostructured substrates called aluminum metafilms (Al-MF), obtained by electrochemical anodization. By varying the dimensions of the Al-MF, it was possible to excite SP at determined wavelengths in the range $\sim 420 - 770$ nm. Increases in temperature (T) and changes in electrical resistivity (ρ) of Al-MF were recorded when irradiated with different wavelengths.

2. Experimental details

For the synthesis of the nanostructured substrates, Al foils (Sigma Aldrich, 0.25 mm thick, 99.999% purity) were used, which were annealed in an H₂ atmosphere at 600°C for 6 hrs. Subsequently, they were electropolished in an electrochemical cell using as electrolyte a solution of perchloric acid and ethanol in a ratio of 5:1 vol., applying voltages of 18 V for 2 min maintaining a temperature of $\sim 3^\circ\text{C}$, in this way, it is possible to obtain a homogeneous surface like the one shown in Fig. 1b).

In the anodization process graphite was used as the cathode and Al as the anode. The anodizing voltages were in the range of 130-250 V supplied by an adjustable DC power source (BK PRECISION model 9185B). The electrolytes used were chosen depending on the applied anodizing voltage [19].

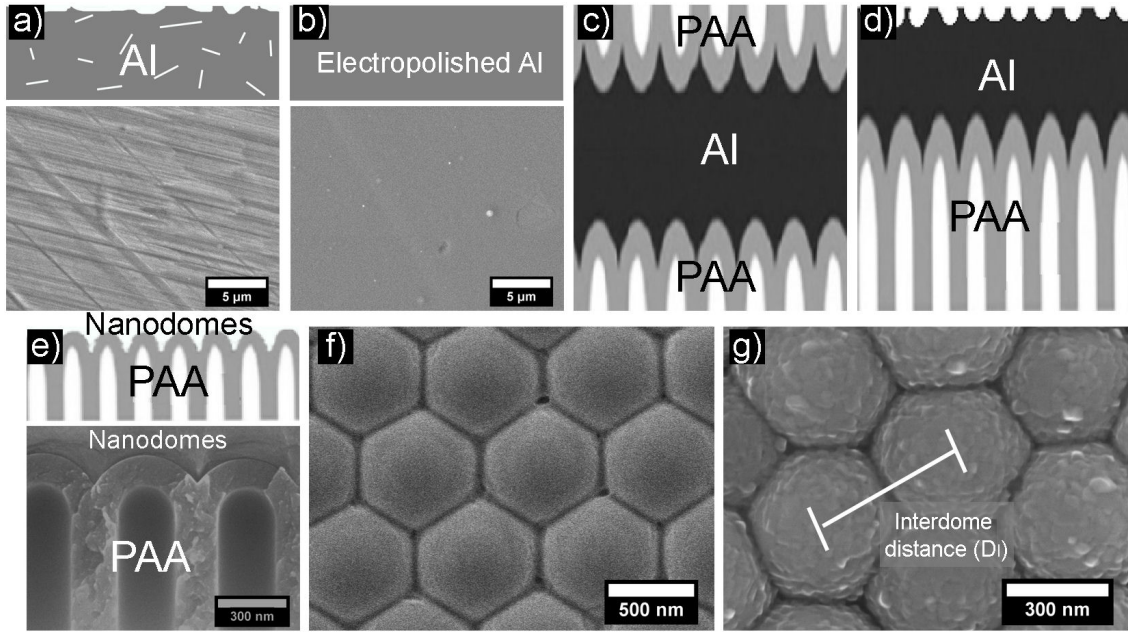


FIGURE 1. Schematic representation and SEM micrographs of the Al-MF synthesis process. a) Al foil without treatment. b) Electropolished Al foil. c) PAA obtained after the anodization process. d) Elimination of the PAA. e) Cross-section and f) Top view of the nanostructured substrates (nanodomains). g) Al film deposited on a nanostructured substrate (Al-MF).

From the anodization process, a type of Al oxide known as Porous Anodic Alumina (PAA) was obtained (see Fig. 1c)). Subsequently, using a solution of NaOH (2.5M) and HCl (20% weight), the PAA was eliminated from one of the faces of the foil; afterward, the residual Al was removed with a solution of CuCl_2 (0.5M) (Fig. 1d)). With this process, the nanostructured substrate (nanodomains), shown in Figs. 1e) and 1f), is obtained.

On the nanodomains (Fig. 1f)) a thin film of Al of ~ 50 nm thick was deposited by thermal evaporation using pressures of $\sim 5 \times 10^{-6}$ torr, thus obtaining what we denominated Al-MF (Fig. 1g)). Its morphology was evaluated using a field emission scanning electron microscope (SEM) JEOL 7600F equipped with an energy dispersive x-ray spectrometer (EDS). The geometric parameters of the Al-MF, such as the interdomain distance (D_I) (Fig. 1g)) were obtained using the Image J software [22]. After, employing a UV-Vis spectrophotometer (UV-2600 Shimadzu Corporation), the specular reflectance measurements were performed at an angle of incidence of 8° in a range of 190-1400 nm.

The measurements of T as a function of the intensity of incident radiation were carried out at a pressure of $\sim 5 \times 10^{-3}$ torr, using a K-type thermocouple of ~ 0.2 mm diameter attached to the sample using silver paint (Colloidal silver paste-EMS). The samples were irradiated in an area of ~ 0.8 mm² using monochromatic CW laser light sources of 445, 532 and 650 nm, varying the incident intensity in an interval of $0 - 4 \times 10^{18}$ photons/(s)cm² (Maximum power of the lasers). Finally, measurements of ρ as a function of T were carried out in the range of ~ 100 -370 K, using the four-terminal sensing, in darkness and under an intensity of

1×10^{16} photons/(s)cm² using the three wavelengths. For these measurements, the maximum light intensity was chosen monitoring the electrical resistance in situ while increasing the intensity and was stopped when we detected a minimum change; with this procedure we think the overheating is minimized.

3. Results and discussion

In Fig. 2a), an SEM micrograph of an Al film deposited on a non-texturized substrate (glass) is shown, while in Figs. 2b) and 2c) Al films deposited on texturized substrates (nanodomains) are shown. In these last two cases, it can be seen that the Al film follows the morphology of the substrate.

The values of the interdomain distance (D_I) obtained from the SEM images (Fig. 1g)) were in the range of $415.5 \pm 57.8 - 786.9 \pm 90.3$ nm. The D_I value depends on the applied anodizing voltage [19-21].

In Fig. 3a) the reflectance spectra as a function of the wavelength of Al-MF with different D_I values are shown. In all cases, minima are observed in the $\sim 420 - 770$ nm wavelength range attributed to first-order surface plasmon resonances (SPR) [1]. The position of these minima can be calculated using as a first approximation the electromagnetic wave coupling model and SPR in two-dimensional periodic arrays with hexagonal geometry, given by [24]:

$$\frac{\varepsilon_m(\lambda)\varepsilon_d}{\varepsilon_m(\lambda) + \varepsilon_d} = \sin^2\theta + \frac{2}{\sqrt{3}}\frac{\lambda}{D_I}(2i + j)\sin\theta + \frac{4}{3}\frac{\lambda^2}{D_I^2}(i^2 + j^2 + ij) \quad (1)$$

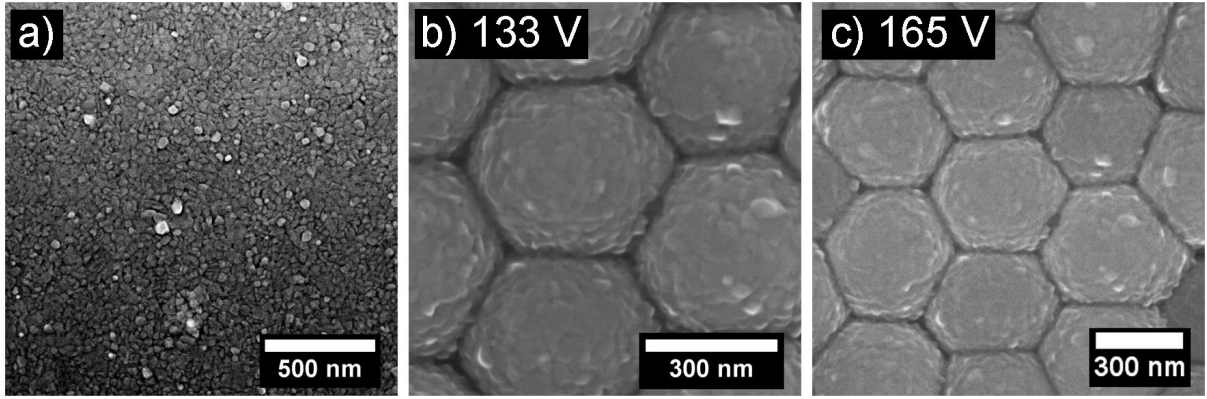


FIGURE 2. SEM images of 50 nm thick Al films on a) Non-texturized substrate (glass), b) and c) Texturized substrates with different anodizing voltages.

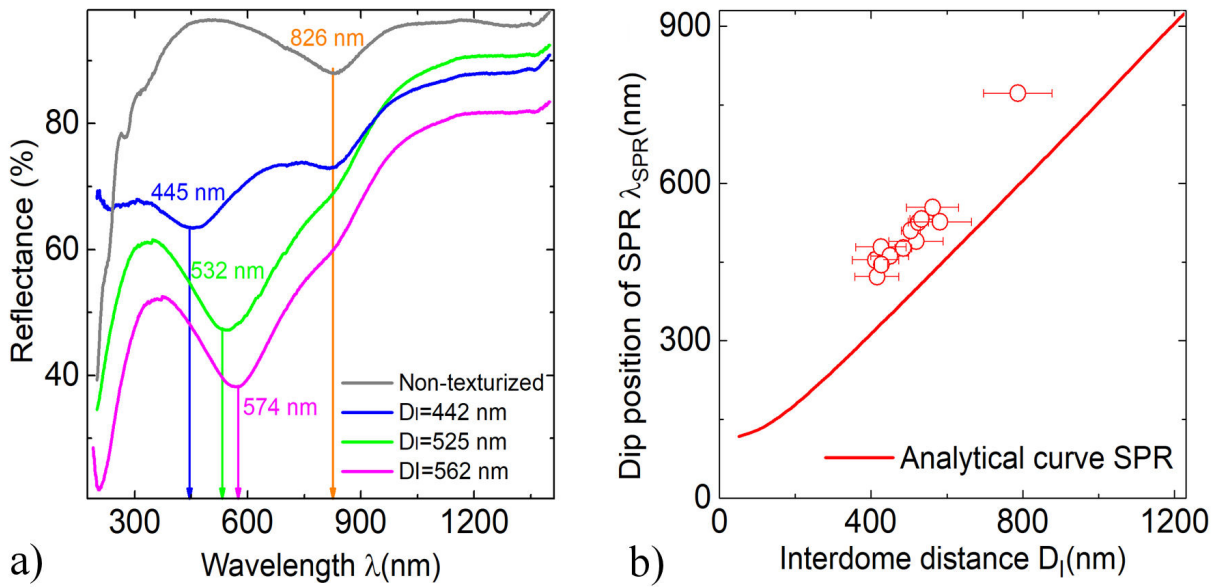


FIGURE 3. a) Reflectance spectra of Al-MF with different D_I . The results for the non-texturized Al film (gray curve) are shown for comparison. b) Experimental data obtained from Al-MF. The analytical curve of SPR (red curve) was performed using the model given by Eq. (1) with an incidence of 8° and the optical constants for Al reported in [23].

where ε_m and ε_d are the dielectric functions of the metal and the dielectric (in our case air, $\varepsilon_d = 1$), respectively; θ is the angle of incidence of the electromagnetic waves, D_I is the period of the array (in our case the interdome distance) and i, j the orders of dispersion. In Fig. 3b), experimental data corresponding to the dip position observed in the reflectance spectra of Al-MF as well as its respective theoretical curve obtained from Eq. (1) [20] are shown.

As shown in Fig. 3a), the position of the minima corresponding to SPR (λ_{SPR}) in the reflectance spectra depends on the dimensions of the D_I . In addition, another dip is observed in all samples at 826 nm related to IT in Al [25,26]. It is worth mentioning that the theoretical model given by Fig. (1) reasonably follows the experimental results (Fig. 3b)). This behavior has also been observed in Ag and Pb metafilms [20]; which demonstrates the possibility of the excitation of surface plasmons in different texturized metals.

For measurements of T as a function of the intensity of incident radiation, Al-MF were synthesized with $\lambda_{\text{SPR}} = 445$ nm and $\lambda_{\text{SPR}} = 532$ nm. According to the results shown in Fig. 4, the increases in T are in the range of 16 – 204 K considering the ambient T (~ 294 K). For the case of the non-texturized Al film (Fig. 4a)), the maximum reached temperature was ~ 316 K using an incident three wavelength of 650 nm ($\lambda_{\text{inc}} = 650$ nm); while for Al-MF with $\lambda_{\text{SPR}} = 445$ nm and $\lambda_{\text{SPR}} = 532$ nm (Figs. 4-b) and 4-c)), the reached temperatures were ~ 432 K and ~ 498 K, respectively. In these last two cases, the increase in T by radiation was greater compared to the non-texturized Al film. In particular, overheating occurs when Al-MF is illuminated with a wavelength close to or equal to its SPR, that is, when $\lambda_{\text{inc}} \approx \lambda_{\text{SPR}}$. Under these conditions, the SP decays in a non-radiative way, generating hot electrons [16] that transfer their energy to the phonons, thus increasing T locally [5].

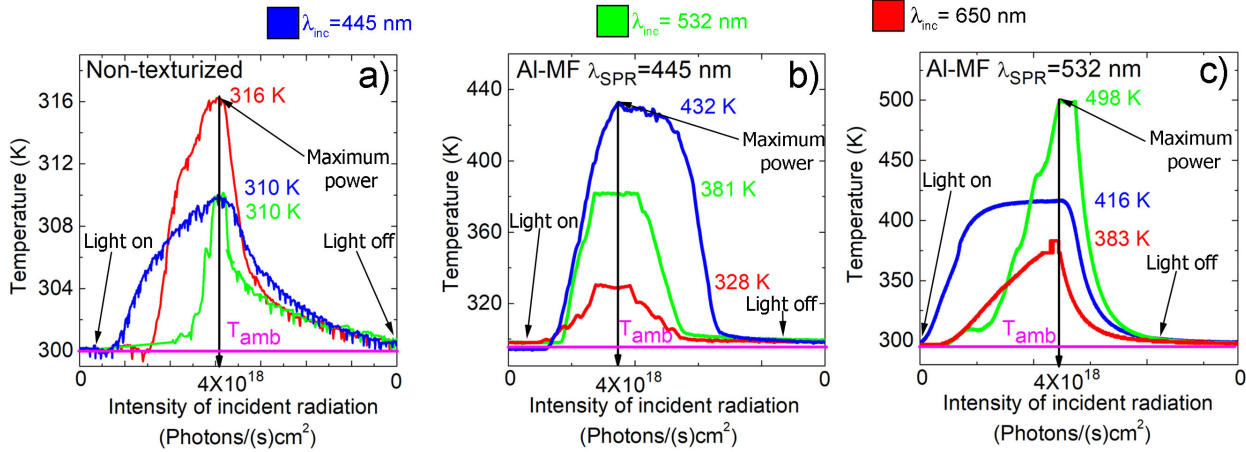


FIGURE 4. T curves as a function of the intensity of incident radiation in a) Non-texturized Al film. Al-MF with b) $\lambda_{SPR} = 445$ nm and c) $\lambda_{SPR} = 532$ nm. The intensity of light begins increasing from zero (Light on) up to a maximum intensity of 4×10^{18} photons/(s)cm² (Maximum power), then it is decreased again to zero (Light off); the total process made in a time of 1 minute, such as is observed in the horizontal axis. The color of the curves corresponds to the shown wavelengths.

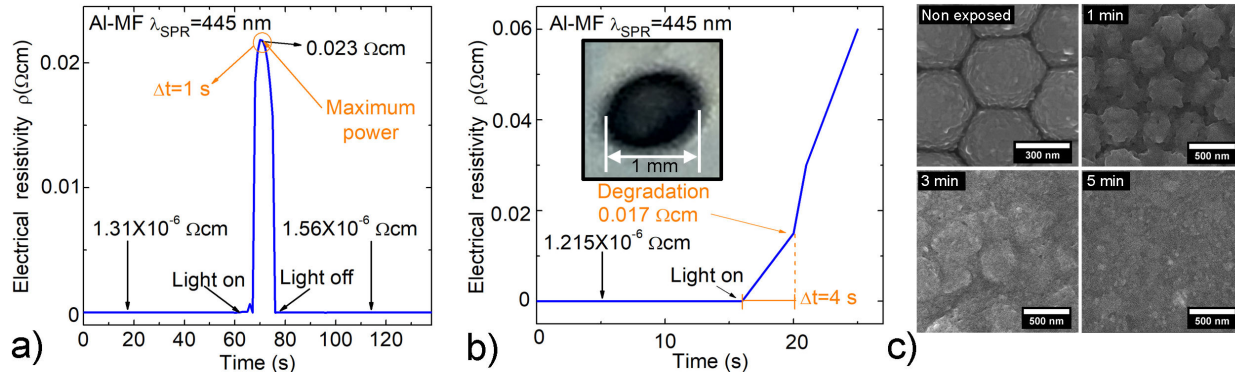


FIGURE 5. Al-MF ρ curves with $\lambda_{SPR} = 445$ nm irradiated with an intensity of $\sim 4 \times 10^{18}$ photons/(s)cm² and a) $t_{exp} = 1$ s and b) $t_{exp} > 4$ s; the inset image belongs to the photograph of a sample damaged by local overheating. The samples were progressively irradiated (Light on) to the laser's maximum power and back to darkness (Light off) c) SEM images from the morphology evolution of an Al-MF irradiated at the different t_{exp} shown in the text.

Measurements of ρ as a function of radiation exposure time (t_{exp}) were performed using an $\lambda_{inc} = \lambda_{SPR} = 445$ nm with power of 4×10^{18} photons/(s)cm². As shown in Fig. 5a), when t_{exp} is ~ 1 s there is an increase in ρ from $\sim 1.3 \times 10^{-6}$ Ω cm to 2.3×10^{-2} Ω cm. In this case, the Al-MF does not show notable deterioration; in addition, its ρ returns approximately to the initial value ($\sim 1.5 \times 10^{-6}$ Ω cm) before being exposed to radiation. On the other hand, in Fig. 5b) it is observed that if the t_{exp} is greater than 1 s, the value of ρ continues to increase due to local overheating in the sample. In particular, at $t_{exp} = 4$ s, a change in the slope of ρ is observed due to the degradation and subsequent evaporation of Al-MF (see inset Fig. 5b)); in this case, ρ does not return to its initial value when irradiation is ceased.

Figure 5c) shows SEM images of the evolution of the morphology of an Al-MF with $\lambda_{SPR} = 445$ nm when irradiated with an $\lambda_{inc} = 445$ nm at a power of 4×10^{18} photons/(s)cm² to a different t_{exp} . The change in its appearance (degradation) due to local overheating is clearly observed.

Locally, the temperatures reached by overheating due to non-radiative decay of SP are estimated to be ~ 933 K (melting point of Al), although it has been reported that the melting point of Al may decrease as the size of the particle decreases (~ 3 K for a particle radius of ~ 40 nm) [27], in our case we estimate that the effect must be negligible since the thickness of our film is 50 nm and continuous. Recently, it has been shown that by the excitation of SP in Al nanoparticles, it is possible to achieve a T of ~ 975 K [15].

To qualitatively show the increase in T in located areas, a drop of water of 1 cm in diameter was placed on an Al-MF with $\lambda_{SPR} = 445$ nm and it was irradiated with an $\lambda_{inc} = 445$ nm with 1 mm diameter at normal incidence, at a power of $\sim 4 \times 10^{18}$ photons/(s)cm². Figure 6 shows the experimental setup, where water vapor bubbles are observed in the area where the laser hits. These appear because temperatures above the boiling point of water are reached (see Fig. 4b)). This fact could be applied to water purification methods [28], to the development of plasmon-mediated nano heat sources

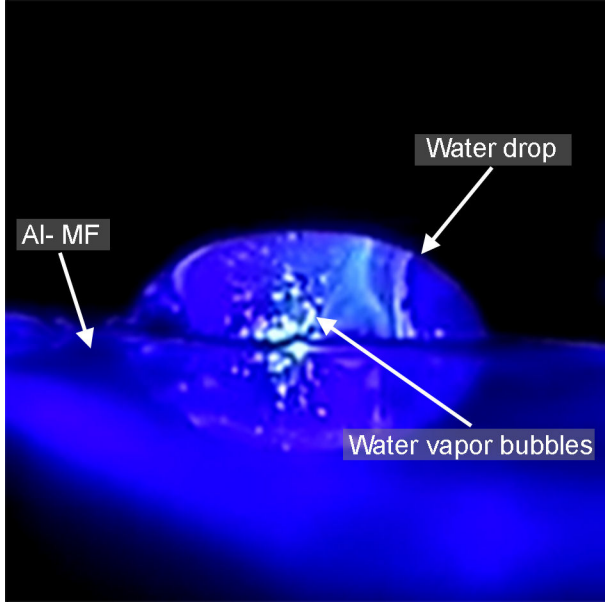


FIGURE 6. Water vapor bubbles induced by overheating in an Al-MF with $\lambda_{\text{SPR}} = 445$ nm when it is irradiated at normal incidence with a laser light source of $\lambda_{\text{inc}} = 445$ nm.

[8], cancer treatments [5], or to generate and control microbubbles, since they are highly relevant in fundamental problems in thermodynamics in the study of local heating of fluids [9]. The following reference shows a video of the observed phenomenon [29]. When the water vapor bubbles are generated, a sound can be perceived, which we assign to a possible phenomenon of nanocavitation [9].

On the other hand, according to Figs. 5a) and 5b), the changes of T in the Al-MF cause a considerable effect on the ρ , it is for this reason that measurements of $\rho(T)$ were carried out irradiating the samples under the same lighting conditions and low intensity 1×10^{16} photons/(s)cm². Figure 7 shows the curves of $\rho(T)$ for a non-texturized film (reference sample) (Fig. 7a) and Al-MF with $\lambda_{\text{SPR}} = 445$ nm and $\lambda_{\text{SPR}} = 532$ nm (Figs. 7b) and 7c), respectively).

In Fig. 7, it is observed that ρ decreases when T decreases in all cases, which is the typical behavior in metals [30]. But the linear behavior of ρ as a function of T below the Debye temperature (T_D) is slightly modified (see the reference pink line). We attribute this behavior to the fact that the electron undergoes scattering due to the texturing present in the sam-

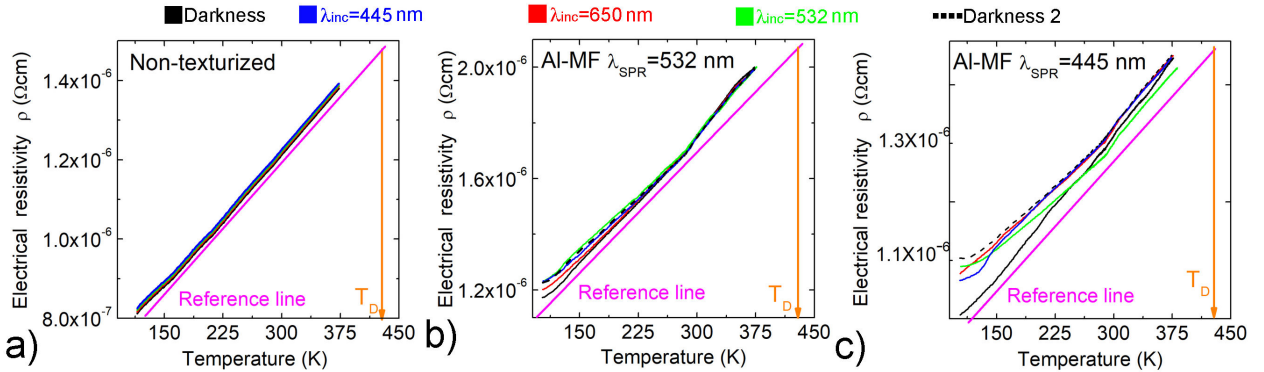


FIGURE 7. Curves of $\rho(T)$ in the dark and using different three wavelengths. a) Non-texturized film. Al-MF ~ 50 nm thick with b) $\lambda_{\text{SPR}} = 445$ nm and c) $\lambda_{\text{SPR}} = 532$ nm. In all cases, a reference line (pink line) and the Al Debye temperature ($T_D = 428$ K, orange line) [30] were placed. The continuous black curve is before the illumination process, the red, green, and blue curves correspond to the illumination with wavelengths of 650, 532, and 445 nm, respectively, while the dashed black curve is after the illumination process.

ples (Figs. 7b) and 7-c)). It is also observed that in a second measurement in darkness in the Al-MF (dashed curve) ρ is slightly higher than the first one (black curve), possibly due to the deterioration caused by local heating when irradiated, even when the used light intensity is low; this effect is more noticeable at low temperatures.

4. Conclusions

The texturing of Al-MF allows a higher efficiency of absorption of light energy that is transformed into heat compared to non-texturized films. When Al-MF are illuminated with λ_{inc} close to or equal to their λ_{SPR} , localized overheating occurs due to non-radiative deexcitation of surface plasmons

and the creation of hot electrons that transfer their energy via phonons and finally heating the Al metafilm. This overheating causes a deterioration of the material and, consequently, a change in the ρ of the Al-MF.

Acknowledgments

We thank Omar Novelo and Lourdes S. Bazán from Laboratorio Universitario de Microscopía Electrónica (LUME-UNAM) for SEM images, Miguel A. Canseco for his assistance in the UV-Vis equipment; Raúl Reyes, Carlos Ramos and Cain González for their technical support in the laboratory (all of them at IIM-UNAM).

1. H. Raether, *Surface Plasmons on Smooth and Rough Surfaces and on Gratings*, (Springer, Berlin, 1988), pp. 4-7.
2. Mark L. Brongersma and Vladimir M. Shalaev, The case for plasmonics, *Appl. Phys.* **328** (210) 440, <https://doi.org/10.1126/science.1186905>
3. E. Ozbay, Plasmonics: Merging Photonics and Electronics at Nanoscale Dimensions, *Science*. **311** (206) 189, <https://doi.org/10.1126/science.1114849>
4. A. Ramazani, F. Shayeganfar, J. Jalilian and N. X. Fang, Exciton-plasmon polariton coupling and hot carrier generation in two-dimensional SiB semiconductors: a first-principles study, *Nanophotonics*. **9** (2020) 337, <https://doi.org/10.1515/nanoph-2019-0363>
5. M. L. Brongersma, N. J. Halas and P. Nordlander, Plasmon-induced hot carriers science and technology, *Nat. Nanotechnology*. **10** (2015) 25, <https://doi.org/10.1038/nnano.2014.311>
6. G. Baffou, F. Cichos and R. Quidant, Applications and challenges of thermoplasmonics, *Nat. Mater.* **19** (2020) 946, <https://doi.org/10.1038/s41563-020-0740-6>
7. X. Meng *et al.*, Nanometals for Solar-to-Chemical Energy Conversion: From Semiconductor-Based Photocatalysis to Plasmon-Mediated Photocatalysis and Photo-Thermocatalysis, *Adv. Mater.* **28** (2016) 6781, <https://doi.org/10.1002/adma.201600305>
8. G. Baffou and R. Quidant, Thermo-plasmonics: using metallic nanostructures as nano-sources of heat, *Laser Photonics Rev.* **7** (2012) 1, <https://doi.org/10.1002/lpor.201200003>
9. G. Baffou, J. Polleux, H. Rigneault and S. Monneret, Super-Heating and Micro-Bubble Generation around Plasmonic Nanoparticles under cw Illumination, *J. Phys. Chem. C*, **118** (2014) 4890, <https://doi.org/10.1021/jp411519k>
10. H. U. Yang *et al.*, Optical dielectric function of silver, *Phys. Rev. B*, **91** (2015) 23, <https://doi.org/10.1103/PhysRevB.91.235137>
11. M. R. Beversluis, A. Bouhelier, and L. Novotny, Continuum generation from single gold nanostructures through near-field mediated intraband transitions, *Phys. Rev. B*, **68** (2003) 115433, <https://doi.org/10.1103/PhysRevB.68.115433>
12. D. Gérard and S. K. Gray, Aluminium plasmonics, *Appl. Phys.* **48** (2015) 18, <https://doi.org/10.1088/0022-3727/48/18/184001>
13. M. W. Knight, N. S. King, L. Liu, H. O. Everitt, P. Nordlander, and N. J. Halas, Aluminum for Plasmonics, *ACS Nano*. **8** (2014) 834, <https://doi.org/10.1021/nn405495q>
14. M. Schwind, B. Kasemo, and I. Zorić, Localized and Propagating Plasmons in Metal Films with Nanoholes, *Nano Lett.* **13** (2013) 1743, <https://doi.org/10.1021/nl400328x>
15. M. Mutlu *et al.*, Thermoplasmonic Ignition of Metal Nanoparticles, *Nano Lett.* **18** (2018) 1699, <https://doi.org/10.1021/acs.nanolett.7b04739>
16. B. Y. Zheng, H. Zhao, A. Manjavacas, M. McClain, P. Nordlander and N. J. Halas, Distinguishing between plasmon-induced and photoexcited carriers in a device geometry, *Nat. Commun.* **6** (2015) 1, <https://doi.org/10.1038/ncomms8797>
17. M. T. Sheldon, J. van de Groep, A. M. Brown, A. Polman and H. A. Atwater, Plasmoelectric potentials in metal nanostructures, *Nanophotonics*. **346** (2014) 828, <https://doi.org/10.1126/science.1258405>
18. Q. Guo *et al.*, Christy, Efficient electrical detection of mid-infrared graphene plasmons at room temperature. *Nat. Mater.* **17** (2018) 986, <https://doi.org/10.1038/s41563-018-0157-7>
19. R. González-Campuzano, M. E. Mata-Zamora, S. López-Romero, and D. Mendoza, Excitation of plasmonic resonances within UV-Vis wavelength range using low-purity aluminum nanoconcave arrays, *Appl. Phys. Lett.* **113** (2018) 221604, <https://doi.org/10.1063/1.5059556>
20. R. González-Campuzano, D. E. Martínez-Lara, and D. Mendoza, Lead plasmonics on texturized substrates: Pb metafilms, *Appl. Phys. Lett.* **117** (2020) 032105, <https://doi.org/10.1063/5.0016131>
21. R. González-Campuzano and D. Mendoza, Excitation of plasmons in self-ordered arrays of aluminum and silver nanocavities within UV-IR spectral range, *J. Phys.: Conf. Ser.* **1221** (2016) 012001, <https://doi.org/10.1088/1742-6596/1221/1/012001>
22. C. A. Schneider, W. S. Rasband, and K. W. Eliceiri, NIH Image to ImageJ: 25 years of image analysis, *Nat. Methods*, **9** (2012) 671 <https://doi.org/10.1038/nmeth.2089>
23. Edward D. Palik, *Handbook of Optical Constants of Solids*, Vol 2., Academic, (New York, 1985), pp. 395-401.
24. E. T. Papaioannou *et al.*, Influence of the magnetic field on the plasmonic properties of transparent Ni anti-dot arrays, *Appl. Phys. Lett.* **19** (2011) 23867, <https://doi.org/10.1063/1.4742931>
25. H. Ehrenreich, H. R. Philipp, and B. Segall, Optical Properties of Aluminum, *Phys. Rev.* **132** (1963) 1918, <https://doi.org/10.1103/PhysRev.132.1918>
26. A. J. Hughes, D. Jones, and A. H. Lettington, Calculation of the optical properties of aluminium, *J. Phys. C: Solid State Phys.* **2** (1968) 102, <https://doi.org/10.1088/0022-3719/2/1/313>
27. J. Sun and S.L. Simon, The melting behavior of aluminum nanoparticles, *Thermochimica Acta* **463** (2007) 32-40, <https://doi.org/10.1016/j.tca.2007.07.007>
28. L. Gomez, V. Sebastian, M. Arruebo, J. Santamaria and S. B. Cronin, Plasmon-enhanced photocatalytic water purification, *Phys. Chem.* **16** (2014) 15111 <https://doi.org/10.1039/C4CP00229F>
29. <https://www.youtube.com/watch?v=bv3aGLV-jmA>
30. C. Kittel, Introduction to Solid State Physics. University of California, Berkeley (John Wiley and Sons, Inc, 2005), pp. 265-267.